Qiao *et al.*
Chinese Journal of Mechanical Engineering (2024) 37:2
https://doi.org/10.1186/s10033-023-00983-6

Chinese Journal of Mechanical Engineering

ORIGINAL ARTICLE

Open Access

Electrochemical Hydrogen Charging on Corrosion Behavior of Ti-6Al-4V Alloy in Artificial Seawater

Yanxin Qiao[1*], Yue Qin[1,2], Huiling Zhou[1], Lanlan Yang[1], Xiaojing Wang[1], Zhengbin Wang[3*], Zhenguang Liu[1] and Jiasheng Zou[1*]

Abstract

This study employs advanced electrochemical and surface characterization techniques to investigate the impact of electrochemical hydrogen charging on the corrosion behavior and surface film of the Ti-6Al-4V alloy. The findings revealed the formation of γ-TiH and δ-TiH_2 hydrides in the alloy after hydrogen charging. Prolonging hydrogen charging resulted in more significant degradation of the alloy microstructure, leading to deteriorated protectiveness of the surface film. This trend was further confirmed by the electrochemical measurements, which showed that the corrosion resistance of the alloy progressively worsened as the hydrogen charging time was increased. Consequently, this work provides valuable insights into the mechanisms underlying the corrosion of Ti-6Al-4V alloy under hydrogen charging conditions.

Keywords Ti-6Al-4V alloy, Hydrogen charging, Electrochemical corrosion, Passive film

1 Introduction

Ocean exploiting is the key to economic development of a country, in which many structural and functional materials are employed. In marine environments, corrosion is one of the major concerns for the safe service of a component or facility made of metals since it can affect service properties leading to catastrophic failure. Titanium and its alloys exhibit superior corrosion resistance due the easy formation of stable protective passive films on the surface [1, 2]. Among titanium alloys, α+β titanium alloys, typically Ti-6Al-4V alloy, have been proven to be technically superior and cost-effective materials with low density, high strength, non-magnetic and good welding performance [3–5], and therefore have been widely used in marine environments [6–8].

However, titanium and its alloys have a well-known shortcoming that they can easily absorb hydrogen so that their mechanical properties [9, 10] and corrosion resistance [11, 12] are seriously deteriorated. In marine environments, the absorbed hydrogen can be generated by the cathodic process of corrosion, especially when titanium alloys are coupled to other metals with lower corrosion potentials [13]. Titanium can react with the absorbed hydrogen to form hydrides due to its high affinity to hydrogen [14]. Many studies have confirmed the formation of TiH_x hydride layers on titanium and its alloys [10, 12, 15–17]. Specially, our previous work has identified δ-TiH_2 and γ-TiH phases, as well as hydrogen-induced cracks, formed in the cathodically polarized Ti-4Al-2V-1Mo-1Fe alloy [9, 11]. It has been

*Correspondence:
Yanxin Qiao
yxqiao@just.edu.cn
Zhengbin Wang
zbwang12s@imr.ac.cn
Jiasheng Zou
zjzoujs@126.com
[1] School of Materials Science and Engineering, Jiangsu University of Science and Technology, Zhenjiang 212003, China
[2] Yangzhou Changelight Co., Ltd, Yangzhou 225012, China
[3] CAS Key Laboratory of Nuclear Materials and Safety Assessment, Institute of Metal Research, Chinese Academy of Sciences, Shenyang 110016, China

found in stainless steels that the absorbed hydrogen and the formed hydrides can deteriorate the corrosion resistance by destroying the protectiveness of passive films via decreasing the thickness, increasing the carrier density or reducing the Cr content of the passive film [18]. However, unlike the widely studied effects of hydrogen-induced deterioration of corrosion resistance of stainless steels, the research on clarifying the role of hydrogen in the corrosion resistance of titanium and its alloys is quite limited up to now, let alone the Ti-6Al-4V alloy.

Therefore, the aim of this study is to clarify the effects of electrochemical hydrogen charging on the corrosion resistance of the Ti-6Al-4V alloy. To this end, hydrogen charging experiment with various times is employed to produce different absorbed hydrogen in the Ti-6Al-4V alloy, electrochemical measurements are performed to evaluate the corrosion behavior, and microstructure characterization and surface analysis are conducted to explain evolution of corrosion resistance with hydrogen charging times.

2 Experimental

2.1 Material Preparation

The material used in this work was a commercial Ti-6Al-4V alloy, whose chemical composition (wt.%) was Al 6.03, V 4.14, C 0.01, O 0.08 and Ti balanced. The as-received Ti-6Al-4V alloy was heat treated at 950 °C for 30 min and then air-cooled in order to obtain the equiaxed microstructure [9]. The samples for microstructure characterization were cut into coupons with dimensions of 10 mm × 5 mm × 3 mm, and then were successively ground to 5000# abrasive paper, etched for 10 s in Kroll's reagent (3 mL HF, 9 mL HNO_3 and 88 mL H_2O), and finally rinsed with distilled water and ethanol.

2.2 Hydrogen Charging Experiment

A hydrogen charging experiment was performed in artificial seawater (pH = 8.2 ± 0.1), which was prepared according to ASTM D1141-98 standard [19], at 25 ± 1 °C controlled by a thermostat water bath. The samples with an exposed area of 1 cm^2 were cathodically charged for different time (0 h, 1 h, 4 h, 8 h and 12 h) at a constant current density of 20 mA/cm^2, using a Gamry reference 600+ electrochemical workstation (Gamry Instruments, Inc. USA). The details of the hydrogen charging experiment had been described in our previous papers [9, 11]. After hydrogen charging experiment, the hydrogen-charged samples were quickly rinsed with distilled water and alcohol, and stored in desiccator for the subsequent tests.

2.3 Electrochemical Measurements

The electrochemical tests were performed for the hydrogen-charged and uncharged samples using a typical three-electrode system in artificial seawater. The hydrogen-charged (or uncharged) Ti-6Al-4V alloys, a Pt foil and saturated calomel electrode acted as the working, counter and reference electrodes, respectively. The electrochemical impedance spectroscopy (EIS) measurements were carried out with a sinusoidal potential perturbation of 10 mV from 100 kHz to 10 mHz at open circuit potential (OCP). The potentiodynamic polarization tests were conducted by sweeping the potential from −0.5 V_{SCE} below the OCP to 2 V_{SCE} with a scan rate of 0.333 mV/s. All electrochemical measurements were repeated at least three times to make the results reproducible.

2.4 SVET and LEIS Measurements

Scanning vibrating electrode technique (SVET, Princeton VersaSCAN, AMETEK Advanced measurement technology) was used to characterize the potential distribution of uncharged and charged Ti-6Al-4V alloys. An 80Ni-20Cr alloy needle with a diameter of 50 μm was utilized as the reference electrode, while the distance between the tip and the sample was set as 150 μm. The working electrode, with a scanning area of 50 μm × 50 μm and a step distance of 2 μm, was also incorporated into the SVET device for the experiment.

The local electrochemical impedance spectroscopy (LEIS) test was carried out on a scanning electrochemical workstation (Princeton VersaSCAN, AMETEK Advanced measurement technology) with a camera system to ensure that the micro-probe was very close to the sample surface. The LEIS micro-probe was a platinum double electrode that moves along two axes at speed of 50 μm/s to adjust the working electrode surface to quantify the local potential gradient in the solution between the alloy surface and the probe, and then i_{loc} (the local alternating current density in the system) was connected. AC interference with an amplitude of 10 mV was applied to working electrode with respect to an OCP. Scanning area of 50 μm × 50 μm with a scan step of 4 μm/s was employed to obtain the LEIS map. Surfer 15 software was used to plot these data into 3D and 2D graphs.

2.5 Surface Characterization and Phase Identification

The surface morphologies of the hydrogen-charged and uncharged samples were observed using field emission scanning electron microscopy (FE-SEM, ZEISS, Germany), and phase constituents was identified with the help of X-ray diffraction (XRD, D/Max 2500 Rigaku Corporation, Tokyo, Japan). The XRD was performed with a Cu

Kα radiation at 10 kV and 35 mA, a scanning speed of 6°/min and an angular step length of 0.02° (2θ). The chemical compositions of the passive films formed on different samples with distinct hydrogen charging times were analyzed by X-ray photoelectron spectroscopy (XPS) using a XPS equipment (ESCALAB 250 xi, Thermo-VG Scientific, MA, USA) with an Al Kα radiation (1486.6 eV). The samples used for the XPS test were immersed in artificial seawater for 3 h and then washed with ethanol and dry in air.

3 Results and Discussion

3.1 Microstructure Characterization

The XRD patterns of the solution-annealing Ti-6Al-4V alloy are shown in Figure 1. The diffraction peaks correspond to the characteristic peaks of α and β phases of the Ti-6Al-4V alloy based on the standard PDF cards. The microstructure of Ti-6Al-4V alloy subjected to solution treatment is displayed in Figure 2. It is clearly seen from Figure 2a that the microstructure is composed of bright α phase (α_p) and dark β transformed structure (β_t). In addition, there are also α_p phases dispersedly distributed within the β_t phase. As seen in Figure 2b showing a more detailed SEM image, a large amount of lath secondary α phase (α_s) is observed within the β_t matrix, which is mainly due to the transformations of β to α_s during the air-cooling process [20]. Such a microstructure for solid solution treated Ti-6Al-4V alloy was also reported by Huang et al. [20].

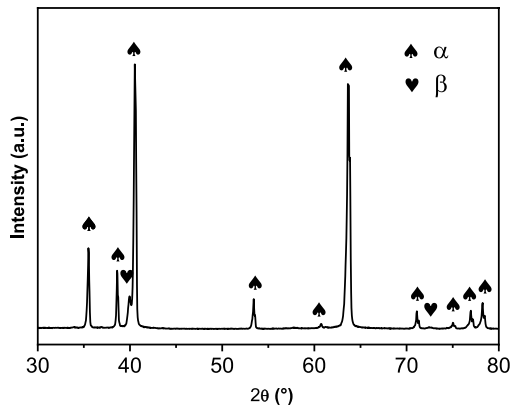

Figure 1 XRD patterns of the solution annealing Ti-6Al-4V alloy

Figure 3a shows the XRD patterns of the hydrogen-charged Ti-6Al-4V alloys. The diffraction peaks are similar to that of the uncharged Ti-6Al-4V alloy shown in Figure 1 on the whole. However, the diffraction peaks at $2\theta = 57.8°$ and 75.0° are also observed, which correspond to the (111) plane of the $TiH_{1.7}$ phase and the (200) plane of $TiH_{1.5}$ phase, respectively [10]. This finding is consistent with Refs. [10, 11], suggesting that two types of titanium hydrides (TiH_x or TiH_2 phases) are formed during the electrochemical hydrogen charging process. Furthermore, the DSC measurements of the hydrogen-charged Ti-6Al-4V alloys are displayed, as shown in Figure 3b, to confirm the formation of hydrides in the Ti-6Al-4V alloys during the hydrogen charging process. Obviously, the hydrogen charging time plays a crucial role in the initial decomposition temperature and total endothermic peak area of hydrides, and the total endothermic peak area increases with prolonging hydrogen charging time, signifying an increase in heat absorption required for hydride formation via alloy decomposition. It indicates higher hydride content in the alloy with increasing charging time. Furthermore, the initial decomposition temperature of the formed hydride also increases, indicating stronger hydride stability [21].

Figure 4 shows the microstructures of the Ti-6Al-4V alloys after hydrogen charging for various times. There is no significant difference in the microstructures among the samples with different hydrogen charging time, and all the sample surfaces remain relatively intact. Similar surface morphology was also observed for the pure titanium charged at 0.5 mA/cm^2 [22].

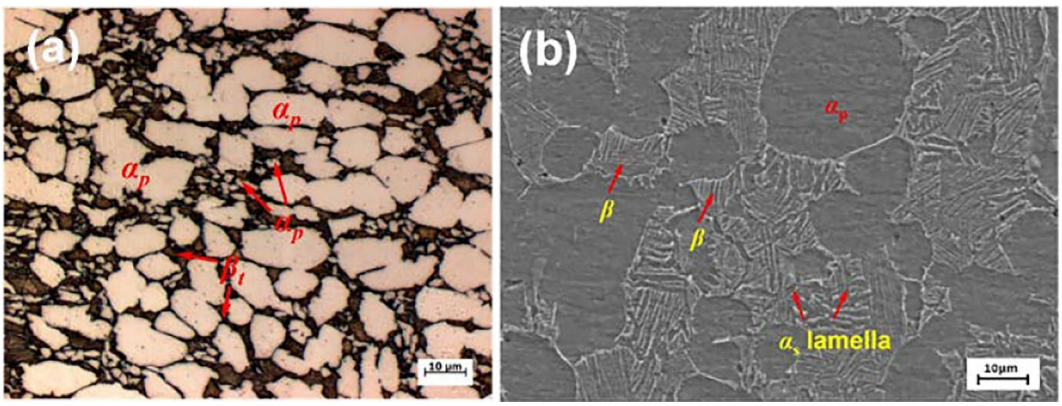

Figure 2 Microstructure of Ti-6Al-4V alloy: **a** Optical microscopic, **b** SEM

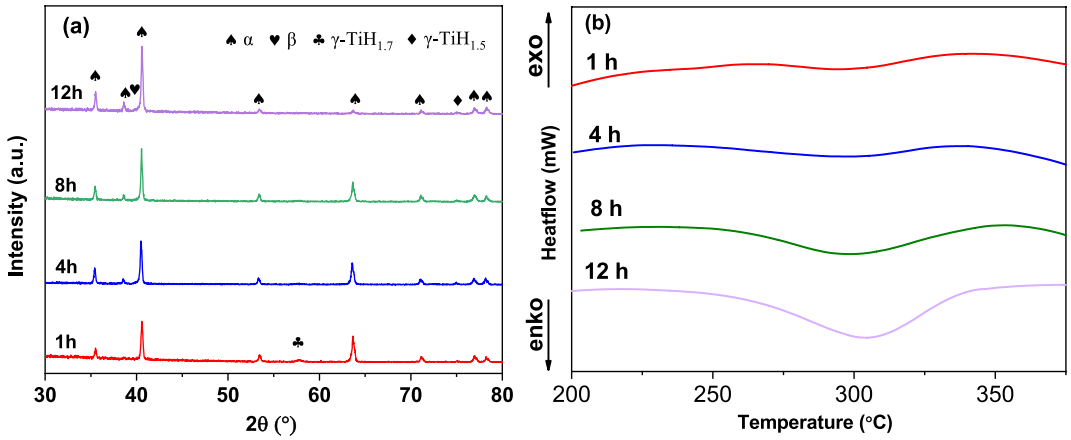

Figure 3 Hydrogen-charged Ti-6Al-4V alloys: **a** XRD patterns, **b** DSC curves

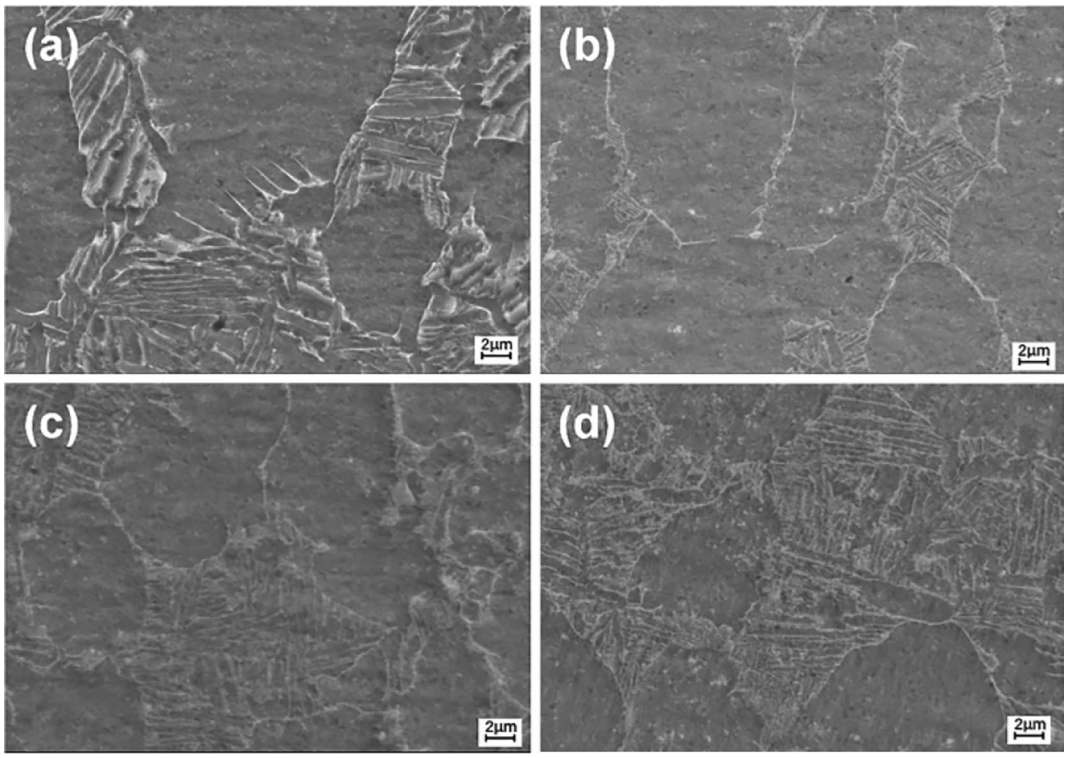

Figure 4 Microstructure of the Ti-6Al-4V alloy after hydrogen charging for various time: **a** 1 h, **b** 4 h, **c** 8 h, **d** 12 h

Figure 5 shows the cross-sectional morphology of a Ti-6Al-4V sample after hydrogen charging for 12 h, revealing the distribution of hydrides in the sample depth and the presence of a surface hydride layer. The hydrides formed near the surface are more prevalent, as compared to those in other regions. The α phase and the α/β phase interface are more susceptible to hydride formation, resulting in needle-like and flocculent hydrides [11], consistent with the XRD results in Figure 3. It is because the α phase and boundaries of α/β phase act as the effective trapping sites for hydrogen, whilst the β phase serves as a short path for hydrogen transport [5, 11].

3.2 Electrochemical Measurements

Figure 6 shows the Nyquist (a) and Bode (b) plots of hydrogen-charged and uncharged Ti-6Al-4V alloys in artificial seawater. The Nyquist plots present unfinished single capacitive reactance arcs, which is the typical characteristic of the EIS spectra for titanium alloys in neutral chloride-containing solutions [8, 19, 23]. The radius of the

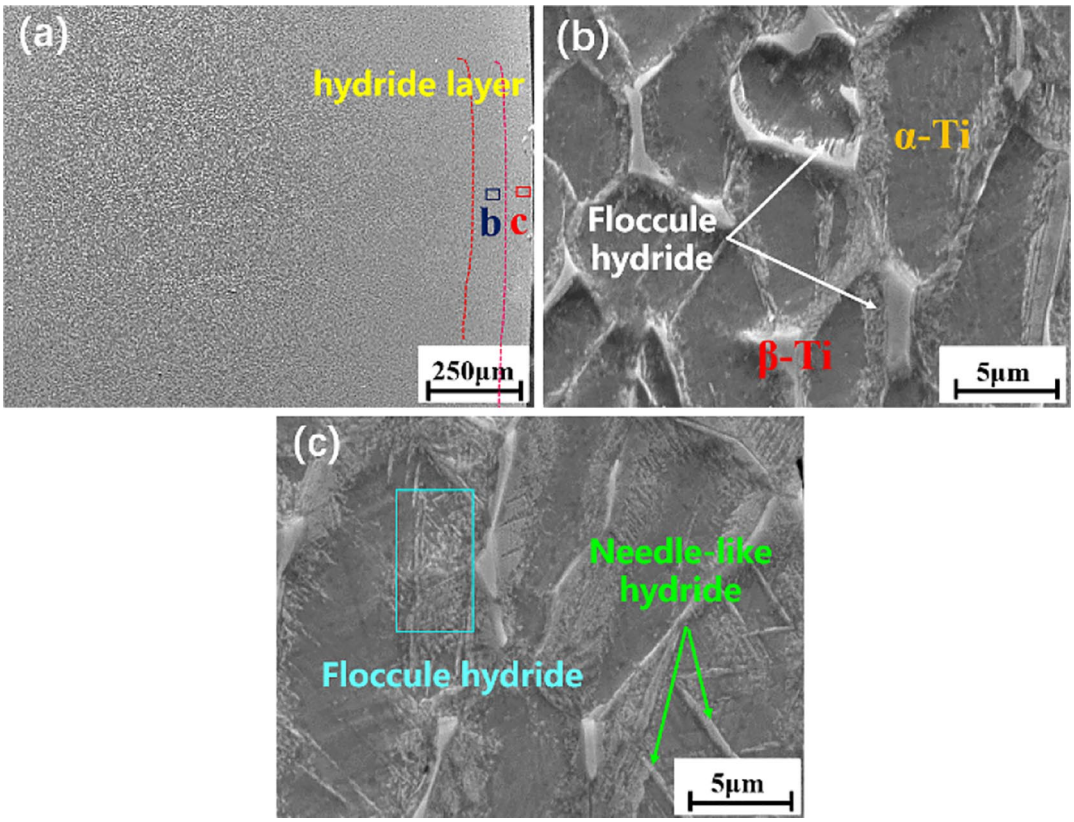

Figure 5 Cross-sectional images of the Ti-6Al-4V alloys after hydrogen charging for 12 h: **a** low-magnified image, **b** and **c** are high-magnified observations to the squared areas in image (**a**)

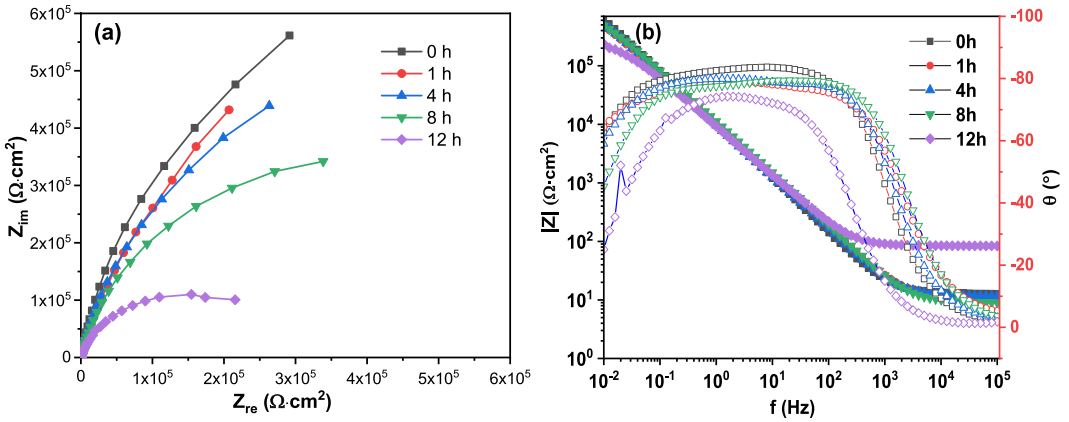

Figure 6 EIS of charged and uncharged Ti-6Al-4V alloys in artificial: **a** Nyquist plots, **b** Bode plots

capacitive arc decreases monotonously with the increasing the hydrogen charging time; especially when the hydrogen charging time is extended to 12 h, the impedance decreases significantly. It indicates that the corrosion resistance is deteriorated by the hydrogen charging. As seen in Figure 6b, the uncharged sample exhibits a phase angle close to 90° at the broad frequency range of 10^{-2} to 10^{3} Hz, which is in good agreement with that found for a Ti-6Al-4V alloy in artificial seawater [8, 19]. In contrast, the hydrogen-charged samples present lower phase angles and narrower frequency ranges, implying that the uncharged Ti-6Al-4V alloy has a stronger capacitive response than the hydrogen-charged ones [24].

All the EIS plots just present one apparent capacitive arc and therefore can be interpreted using the equivalent circuit with one time constant, as shown in Figure 7

in which R_s is the solution resistance, R_p is the polarization resistance, and the constant phase element (CPE, Q) is the capacitance of the surface films [25, 26]. Herein, the CPE, instead of capacitance (C), is used to improve the fitting quality due to the deviation to ideal electric behavior arising from the heterogeneities of surface films [27–30]. Table 1 summarizes the EIS fitting parameters using the equivalent circuit above. As seen in Table 1, the R_p value for the uncharged sample is 1.93×10^6 Ω·cm^2, while it decreases slightly to 1.73×10^6 Ω·cm^2 after 1 h hydrogen charging. The R_p value decreases continuously with prolonging the hydrogen charging time. The minimum R_p value (2.86×10^5 Ω·cm^2) appears after hydrogen charging for 12 h, which accounts for 14.66% of the uncharged sample. It is well-accepted that the larger the R_p, the higher the corrosion resistance. Accordingly, the decrease in R_p demonstrates that the hydrogen charging is harmful for the corrosion resistance of Ti-6Al-4V alloy. Besides, the n value, which is an adjustable CPE power factor, decreases with the hydrogen charging time, indicating that the passive film protectiveness is weakened [31].

Furthermore, the capacitance (C) of the passive film can be calculated from Q using Eq. (1), which can be used to estimate the thickness (d) of passive film using Eq. (2):

$$C = (R^{1-n}Q)^{1/n}, \tag{1}$$

$$C = \frac{\varepsilon_0 \varepsilon A}{d}, \tag{2}$$

where ε_0 is the vacuum permittivity (8.85×10^{-14} F·cm^{-1}), ε is the dielectric constant of the oxide, and A is the effective area. Generally, the passive film formed on titanium alloys is mainly composed of TiO_2, so the $\varepsilon=65$ of TiO_2 can be adopted in this research [32]. The estimated values of d show that the passive films formed on all Ti-6Al-4V alloys are typically ~ 1 nm thick, as seen in Table 1. However, it is difficult to obtain the accurate values for the passive film thickness using the capacitance since the dielectric constant varies when the composition of the passive film changes.

Figure 8 shows the potentiodynamic polarization curves of the different Ti-6Al-4V alloys in artificial seawater. All the samples exhibit spontaneous passive behavior, the typical electrochemical corrosion behavior of titanium and its alloy in neutral solutions [11]. However, the polarization behaviors among various samples differ in the cathodic potential region, corrosion potential (E_{corr}) and high potential region (above 1.0 V_{SCE}). As the hydrogen charging time increases, the cathodic curves move to the direction of higher current density, indicating that the cathodic reactions are facilitated. It is possible that the absorption of hydrogen and the formation of hydrides make the surface more energetic, thus promoting the cathodic reactions. According to the mixed potential theory, the facilitation of cathodic reactions can lead to a noble shift in E_{corr}. This is consistent with the results for titanium alloys in a 3.5 wt.% NaCl solution [33–35], as shown in Table 2. Additionally, the

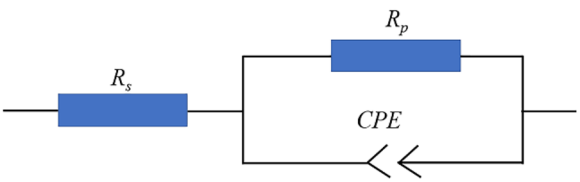

Figure 7 Equivalent circuit model used to fitting the EIS data

Table 1 The EIS data of charged and uncharged Ti-6Al-4V alloys

t (h)	R_s (Ω·cm^2)	R_p (Ω·cm^2)	Q (Ω^{-1}·S^n·cm^2)	*n*	*d* (nm)
0	13.15	1.93×10^6	2.21×10^{-5}	0.93	1.81
1	10.10	1.73×10^6	2.07×10^{-5}	0.91	1.80
4	11.67	1.36×10^6	2.01×10^{-5}	0.89	1.76
8	8.94	8.23×10^5	1.75×10^{-5}	0.89	1.64
12	8.32	2.86×10^5	2.27×10^{-5}	0.85	1.12

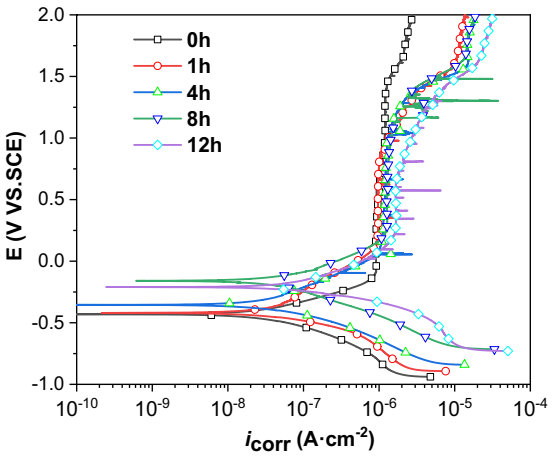

Figure 8 Potentiodynamic polarization curves of hydrogen-charged and uncharged Ti-6Al-4V alloys in artificial seawater

Table 2 Electrochemical results derived from the potentiodynamic polarization curves

t (h)	E_{corr} (V_{SCE})	i_{corr} (A/cm^2)	E_{pit} (V_{SCE})	i_{pass} (A/cm^2)
0	−0.43 ± 0.01	(4.62 ± 0.08) × 10^{-8}	−0.08 ± 0.02	(9.05 ± 0.06) × 10^{-7}
1	−0.42 ± 0.02	(4.98 ± 0.10) × 10^{-8}	0.22 ± 0.03	(9.76 ± 0.11) × 10^{-7}
4	−0.35 ± 0.02	(5.32 ± 0.17) × 10^{-8}	0.25 ± 0.06	(1.15 ± 0.14) × 10^{-6}
8	−0.16 ± 0.01	(6.35 ± 0.15) × 10^{-8}	0.26 ± 0.05	(1.27 ± 0.09) × 10^{-6}
12	−0.21 ± 0.02	(9.19 ± 0.22) × 10^{-8}	0.25 ± 0.04	(1.67 ± 0.17) × 10^{-6}

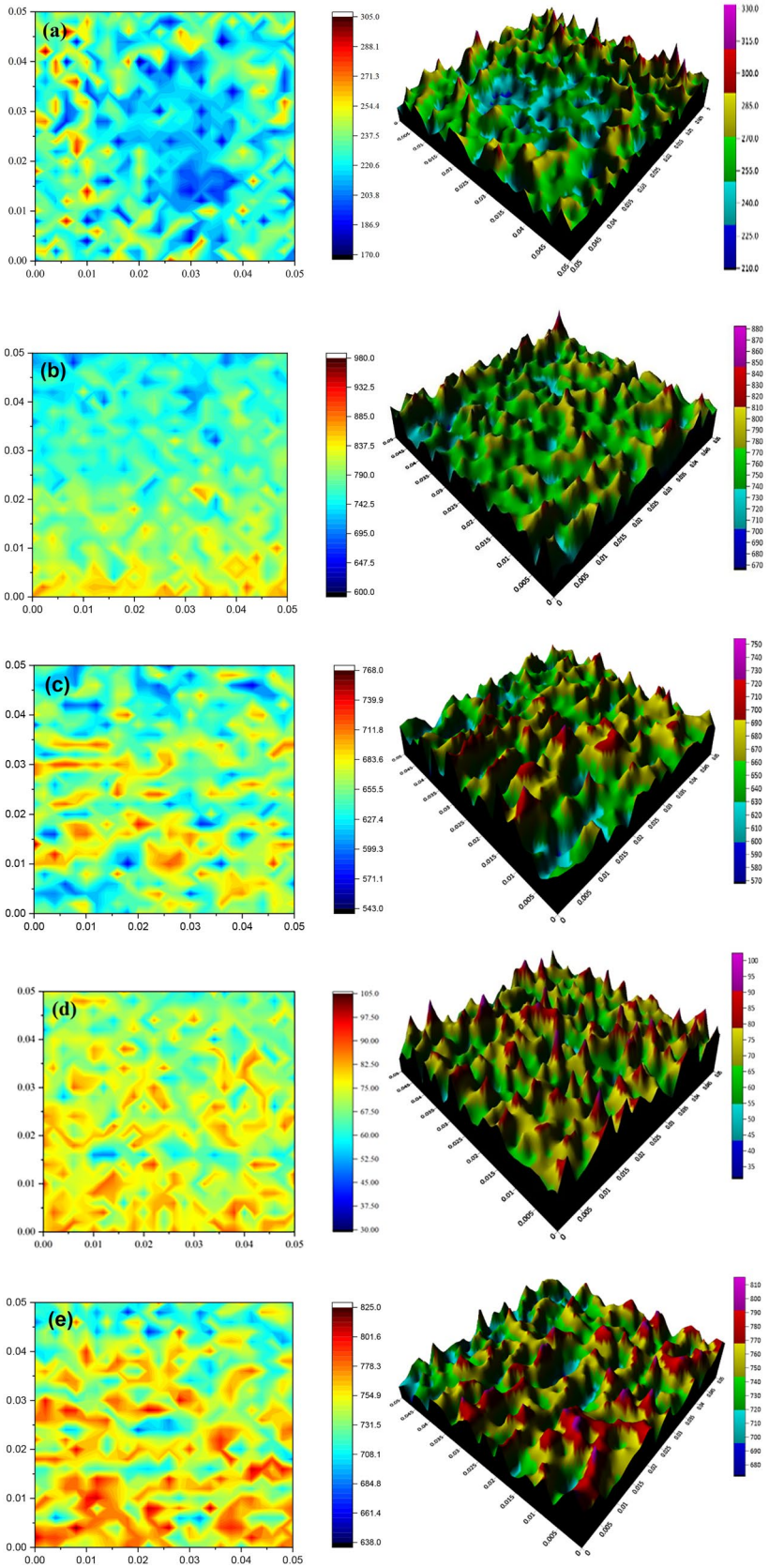

Figure 9 The 2D and 3D SVET maps of Ti-6Al-4V alloys after hydrogen charging for various time in artificial seawater: **a** 0 h, **b** 1 h, **c** 4 h, **d** 8 h, **e** 12 h

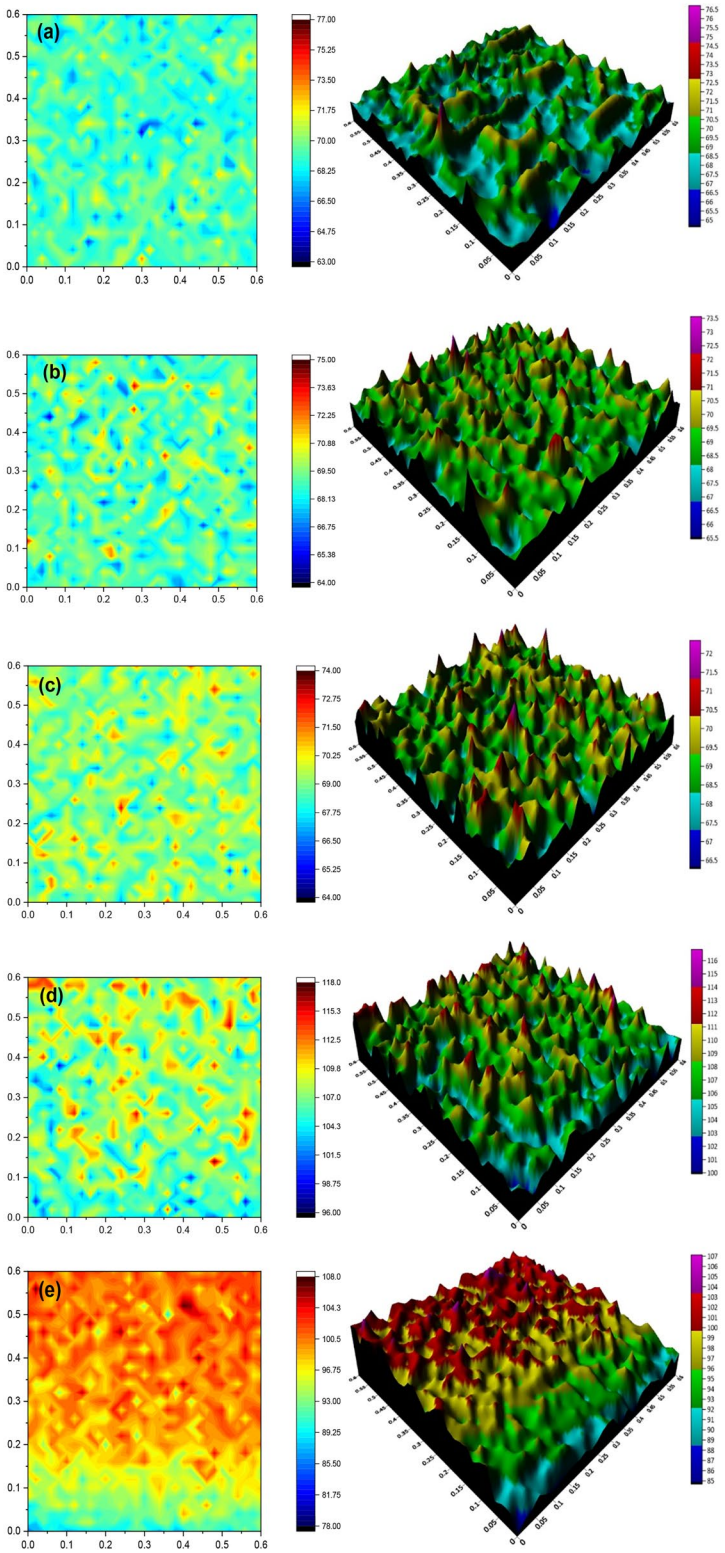

Figure 10 The 3D and 2D LEIS maps of Ti-6Al-4V alloys after hydrogen charging for various time in artificial seawater: **a** 0 h, **b** 1 h;, **c** 4 h, **d** 8 h, **e** 12 h

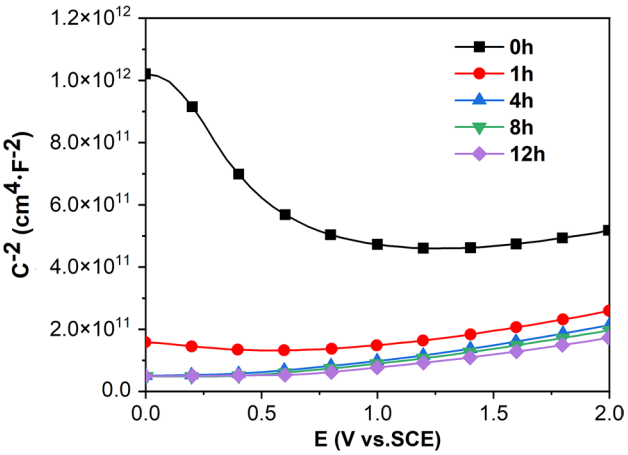

Figure 11 Mott-Schottky plots of the hydrogen-charged and uncharged Ti-6Al-4V alloys in artificial seawater

Table 3 The donor densities for passive films on the hydrogen-charged and uncharged Ti-6Al-4V alloys

Hydrogen charging time (h)	0	1	4	8	12
N_D ($cm^{-3}{\cdot}10^{19}$)	4.22	4.54	4.73	4.91	6.10

uncharged sample displays exceptional stability in the passive region, exhibiting no discernible pitting behavior even at potentials above 2.0 V_{SCE}. This indicates the superior pitting corrosion resistance of the Ti-6Al-4V alloy. For the hydrogen-charged samples, the presence of many small current transients in the passive region suggests the formation of metastable pits [36, 37]. Table 2 also exhibits the corrosion parameters of current density (i_{corr}), passive potential (E_{pit}) and the passive current density (i_{pass}). All the hydrogen-charged samples, regardless of the charging time, have higher i_{pass} and narrower passive region in comparison with the uncharged sample. The shrinking of the passive region after hydrogen charging may be due to the difference in the composition and properties of the passive film [38–40]. The electrochemical results indicate that hydrogen charging can worsen the stability of the passive film formed on Ti-6Al-4V alloy and thus deteriorate the corrosion resistance.

3.3 SVET Measurements

The potential distribution of uncharged and hydrogen-charged Ti-6Al-4V alloys obtained by the SVET test is depicted in Figure 9. It is evident that uneven local anode and cathode emerge on the surface of the Ti-6Al-4V alloy. The cathode area and anode area of the metal surface are in a state of constant flux, exhibiting the traits of local corrosion. With increasing the hydrogen charging time, the surface potential shifts gradually towards the positive side, and the cathode and anode become more pronounced, indicating a more severe tendency towards localized corrosion.

3.4 LEIS Measurements

Figure 10 shows LEIS 3D and 2D maps of Ti-6Al-4V alloys with different hydrogen charging time in artificial seawater. The color intensity indicates the potential distribution on the sample surface, with the gradient of colors ranging from blue to red based on potential magnitude. As hydrogen charging time increases, the difference between red and blue values becomes more pronounced, indicating larger potential differences on the sample surface and a more severe tendency for localized corrosion. This finding is consistent with the results of SVET testing.**Figure 10** The 3D and 2D LEIS maps of Ti-6Al-4V alloys after hydrogen charging for various time in artificial seawater: **a** 0 h, **b** 1 h;, **c** 4 h, **d** 8 h, **e** 12 h

3.5 Mott-Schottky Curves

Figure 11 presents the Mott-Schottky plots for the hydrogen-charged and uncharged Ti-6Al-4V alloys in artificial seawater. Two linear regions are obvious in all plots, with a positive and negative slope characterized by different capacitance behavior. According to the Mott-Schottky theory, the relationship of space-charge capacitance and the semiconductor behavior of the passive film can be given by the following equations, respectively:

$$\frac{1}{C^2}=\frac{2}{\varepsilon\varepsilon_0 eN_D}\left(E-E_{FB}-\frac{\kappa T}{e}\right), \tag{3}$$

$$\frac{1}{C^2}=\frac{-2}{\varepsilon\varepsilon_0 eN_A}\left(E-E_{FB}-\frac{\kappa T}{e}\right), \tag{4}$$

where ε is dielectric constant of the passive film (65 for TiO_2 [32]), ε_0 is vacuum permittivity (8.85×10^{-14} $F{\cdot}cm^{-1}$), e is electron charge (1.60×10^{-19} C), N_D/N_A is the donor/acceptor density in the passive film, k is Boltzmann constant (1.38×10^{-23} $J{\cdot}mol^{-1}{\cdot}K^{-1}$), T is temperature, E is applied potential and E_{FB} is flat band potential. Accordingly, it can be confirmed that the passive film formed on the hydrogen-charged samples is characterized as a n-type semiconductor due to the positive slopes in Figure 6 [41, 42]. In the present case, the defects of oxygen vacancies could serve as the dominated charge carriers since they have lower formation energy than Ti^{3+} interstitials [43, 44]. The donor density (N_D) calculated from the Mott-Schottky data is listed in Table 3. It

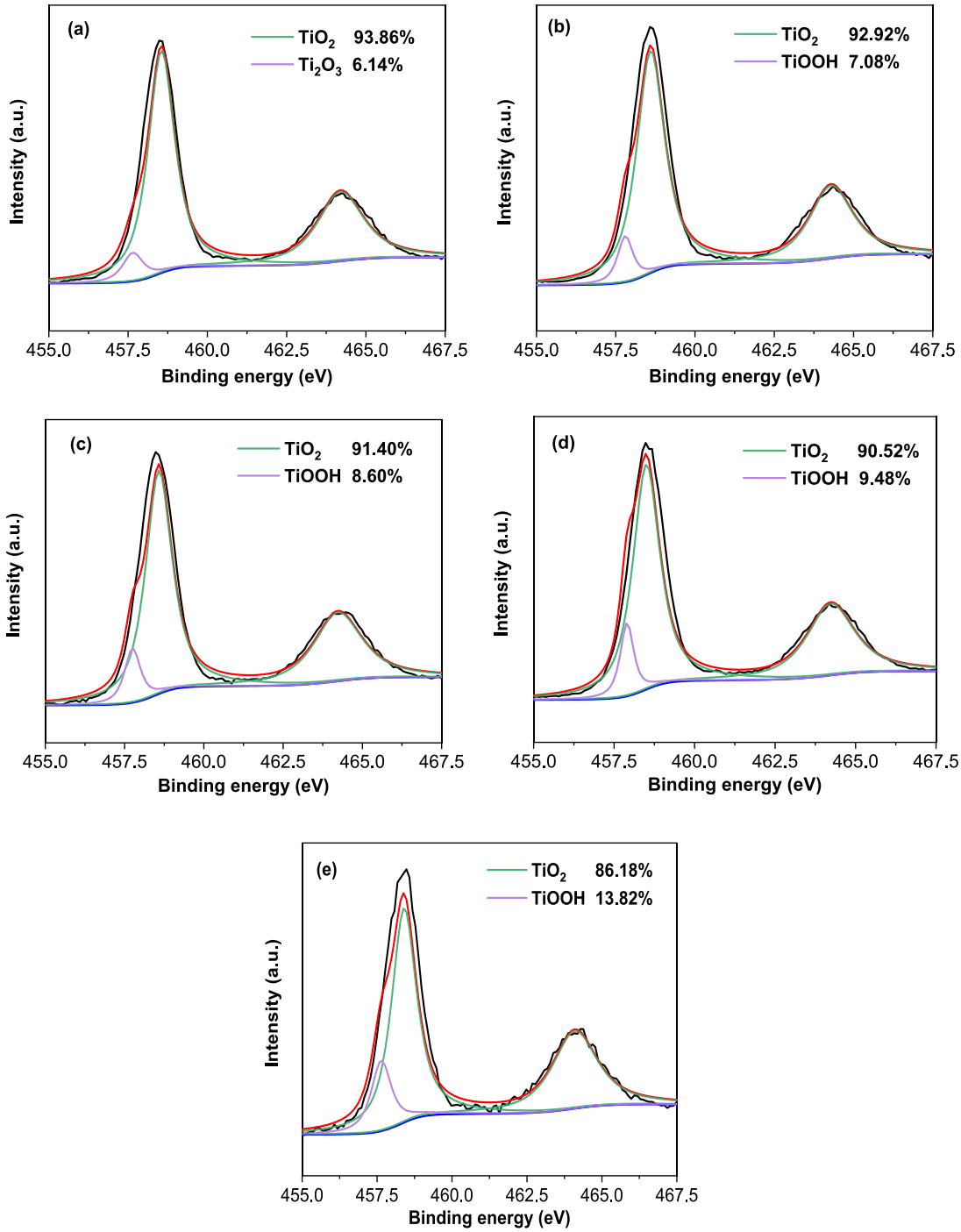

Figure 12 Detailed Ti 2p XPS spectra of the **a** uncharged and hydrogen-charged Ti-6Al-4V alloys for **b** 1 h, **c** 4 h, **d** 8 h, **e** 12 h

shows that the donor density increases with the hydrogen charging time, indicating that the passive film is less protective under hydrogen charging conditions and revealing a porous and highly conductive passive film.

3.6 XPS Characterization

The compositions of the surface films on the hydrogen-charged and uncharged samples formed after immersion in artificial seawater for 3 h, identified by XPS analyses, are

shown in Figure 12. The detailed XPS spectra of Ti 2p can be divided into the peaks of Ti^{4+} (TiO_2) and Ti^{3+} (Ti_2O_3 or TiOOH) [45, 46]. The formation of a passive film with such compositions on titanium is based on the following reactions [47, 48]:

$$Ti \rightarrow Ti^{3+} + 3e, \tag{5}$$

$$2Ti^{3+} + 3H_2O \rightarrow 2Ti_2O_3 + 6H^+, \tag{6}$$

$$Ti_2O_3 + H_2O \rightarrow 2TiO_2 + 2H^+ + 2e, \tag{7}$$

$$Ti^{3+} \rightarrow Ti^{4+} + e, \tag{8}$$

$$Ti^{4+} + 2H_2O \rightarrow TiO_2 + 4H^+. \tag{9}$$

The TiO_2 can be transformed to TiOOH with the aid of produced hydrogen, which can be expressed as follows [48]:

$$TiO_2 + H_{abs} \rightarrow TiOOH. \tag{10}$$

As shown in Figure 12, for the uncharged samples, TiO_2 constitutes 93.86% of the passive film. However, when the samples are charged with hydrogen, the content of TiOOH in the passive film increases while the proportion of TiO_2 decreases, indicating that TiO_2 in the passive film is replaced by TiOOH due to the combination of hydrogen atoms [10]. As the hydrogen charging is prolonged, the content of TiO_2 in the passive film decreases further. When the hydrogen charging time reaches 12 h, the content of TiO_2 decreases to 86.18%, while the content of TiOOH increases to 13.82%. It indicates the degradation of protectiveness of the passive film. In a summary, the introduction of hydrogen is detrimental to the corrosion resistance of Ti-6Al-4V alloys since it destroys the protective passive film [22].

4 Conclusions

The current research investigated the effects of electrochemical hydrogen charging on the corrosion resistance of the Ti-6Al-4V alloy. The main conclusions can be drawn as follows.

Hydrogen charging induced the formation of γ-TiH and δ-TiH_2 hydrides, with no other detectable surface changes. This led to the deterioration of corrosion resistance of the Ti-6Al-4V alloy, as evidenced by decrease in polarization resistance, increase in passive current density, and the narrower passive potential region. SVET and LEIS data further supported the enhanced localized corrosion tendency resulting from hydrogen charging. The reduction in corrosion resistance was attributed to the deteriorated protectiveness of the passive film, as indicated by increased donor density and decreased TiO_2 content observed in the passive film using Mott-Schottky and XPS analyses, respectively.

Acknowledgements
Not applicable.

Authors' Contributions
YQ and JZ was responsible for the planning of the content and writing; YQ and LY performed experimental and data curation; XW and ZL analyzed the data; YQ, YQ, HZ and ZW were major contributors in writing the manuscript. All authors read and approved the final manuscript.

Authors' Information
Yanxin Qiao, born in 1980, is currently an associate professor at *School of Materials Science and Engineering, Jiangsu University of Science and Technology, China*. He received his PhD degree on Materials Science and Engineering from *Institute of Metal Research, Chinese Academy of Sciences, China*, in 2009. His current research interests include corrosion and protection, welding, additive manufacturing, wear, etc.
Yue Qin, born in 1995, is currently an engineer at *Yangzhou Changelight Co., Ltd, China*. She received her master degree on Materials Science and Engineering from *Jiangsu University of Science and Technology, China*, in 2021.
Huiling Zhou, born in 1980, is currently an associate professor at *School of Materials Science and Engineering, Jiangsu University of Science and Technology, China*.
Lanlan Yang, born in 1989, is currently an associate professor at *School of Materials Science and Engineering, Jiangsu University of Science and Technology, China*.
Xiaojing Wang, born in 1977, is currently an associate professor at *School of Materials Science and Engineering, Jiangsu University of Science and Technology, China*.
Zhengbin Wang, born in 1989, is currently an associate professor at *CAS Key Laboratory of Nuclear Materials and Safety Assessment, Institute of Metal Research, Chinese Academy of Sciences, China*.
Zhenguang Liu, born in 1986, is currently an associate professor at *School of Materials Science and Engineering, Jiangsu University of Science and Technology, China*.
Jiasheng Zou, born in 1965, is currently a professor at *School of Materials Science and Engineering, Jiangsu University of Science and Technology, China*.

Funding
Supported by National Natural Science Foundation of China (Grant Nos. 52001142, 52005228, 51801218, 51911530211, 51905110), and Young Scientists Sponsorship Program by CAST (Grant No. 2022QNRC001).

Availability of Data and Materials
The data used to support the findings of this study are available from the corresponding author upon request.

Declarations

Competing Interests
The authors declare no competing financial interests.

Received: 2 November 2022 Revised: 1 October 2023 Accepted: 14 November 2023
Published online: 02 January 2024

References

[1] Z B Wang, H X Hu, Y G Zheng, et al. Comparison of the corrosion behavior of pure titanium and its alloys in fluoride-containing sulfuric acid. *Corrosion Science*, 2016, 103: 50–65.

[2] L Liang, Y X Qiao, L M Zhang, et al. Effect of cavitation erosion induced surface damage on the corrosion behavior of TA31 titanium alloy. *Ultrasonics Sonochemistry*, 2023, 98: 106498.

[3] J J Dong, L Fan, H B Zhang, et al. Electrochemical performance of passive film formed on Ti–Al–Nb–Zr alloy in simulated deep sea environments. *Acta Metallurgica Sinica (English Letters)*, 2019, 33(4): 595–604.

[4] S Mironov, Y S Sato, H Kokawa. Friction-stir welding and processing of Ti-6Al-4V titanium alloy: A review. *Journal of Materials Science & Technology*, 2018, 34(1): 58–72.

[5] E Tal-Gutelmacher, D Eliezer. The hydrogen embrittlement of titanium-based alloys. *JOM*, 2005, 57(9): 46–49.

[6] Y Bai, X Gai, S J Li, et al. Improved corrosion behaviour of electron beam melted Ti-6Al–4V alloy in phosphate buffered saline. *Corrosion Science*, 2017, 123: 289–296.

[7] P Qin, Y Chen, Y J Liu, et al. Resemblance in corrosion behavior of selective laser melted and traditional monolithic β Ti-24Nb-4Zr-8Sn alloy. *ACS Biomaterials Science & Engineering*, 2018, 5(2): 1141–1149.

[8] Y X Qiao, D K Xu, S Wang, et al. Corrosion and tensile behaviors of Ti-4Al-2V-1Mo-1Fe and Ti-6Al-4V titanium alloys. *Metals*, 2019, 9(11): 1213.

[9] S Wang, D K Xu, Z Q Zhang, et al. Effect of electrochemical hydrogen charging on the mechanical behavior of a dual-phase Ti-4Al-2V-1Mo-1Fe (in wt.%) alloy. *Materials Science and Engneering A*, 2021, 802: 140448.

[10] S P Liu, Z Zhang, J Xia, et al. Effect of hydrogen pre-charging on mechanical and electrochemical properties of pure titanium. *Advanced Engineering Materials*, 2020, 22: 1901182.

[11] Y X Qiao, D K Xu, S Wang, et al. Effect of hydrogen charging on microstructural evolution and corrosion behavior of a Ti-4Al-2V-1Mo-1Fe alloy. *Journal of Materials Science & Technology*, 2021, 60: 168–176.

[12] Z M Pan, Y Wei, Y Fu, et al. Effect of electrochemical hydrogen charging on the mechanical property and corrosion behavior of Ti-3Mo alloy. *Corrosion Science*, 2022, 200: 110219.

[13] Z Esen, E B Öcal, A Akkaya, et al. Corrosion behaviours of Ti6Al4V-Mg/Mg-Alloy composites. *Corrosion Science*, 2020, 166: 108470.

[14] S Lathabai, B L Jarvis, K J Barton. Comparison of keyhole and conventional gas tungsten arc welds in commercially pure titanium. *Materials Science and Engineering A*, 2001, 299(1–2): 81–93.

[15] J W Kim, E Plancher, C C Tasan. Hydrogenation-induced lattice expansion and its effects on hydrogen diffusion and damage in Ti–6Al–4V. *Acta Materialia*, 2020, 188: 686–696.

[16] X F Li, X F Ma, J Zhang, et al. Review of hydrogen embrittlement in metals: hydrogen diffusion, hydrogen characterization, hydrogen embrittlement mechanism and prevention. *Acta Metallurgica Sinica (English Letters)*, 2020, 33(6): 759–773.

[17] K Videm, S Lamolle, M Monjo, et al. Hydride formation on titanium surfaces by cathodic polarization. *Applied Surface Science*, 2008, 255(5): 3011–3015.

[18] J G Yu, J L Luo, P R Norton. Effects of hydrogen on the electronic properties and stability of the passive films on iron. *Applied Surface Science*, 2001, 177(1–2): 129–138.

[19] Y Q Fu, F Zhou, Q Z Wang, et al. Electrochemical and tribocorrosion performances of CrMoSiCN coating on Ti-6Al-4V titanium alloy in artificial seawater. *Corrosion Science*, 2020, 165: 108385.

[20] S S Huang, Y J Ma, S L Zhang, et al. Influence of alloying elements partitioning behaviors on the microstructure and mechanical properties in α+β titanium alloy. *Acta Metallurgica Sinica*, 2019, 55(6): 741–750.

[21] X Y Chen, R R Chen, X Ding, et al. Effect of phase formation on hydrogen storage properties in Ti-V-Mn alloys by zirconium substitution. *Energy*, 2019, 166: 587–597.

[22] W Wu, J Liu, Z Y Liu, et al. Surface characterization of the commercially pure titanium after hydrogen charging and its electrochemical characteristics in artificial seawater. *Journal of Electroanalytical Chemistry*, 2018, 822: 23–32.

[23] D P Wang, G Chen, A D Wang, Y et al. Corrosion behavior of single- and poly-crystalline dual-phase TiAl-Ti3Al alloy in NaCl solution. *International Journal of Minerals, Metallurgy and Materials*, 2023, 30(4): 689–696.

[24] Z Liu, L M Zhang, W Q Chen, et al. Effect of oxidizing ions on the corrosion behavior of SiN stainless steel in high-temperature nitric acid solution. *Electrochimica Acta*, 2023, 442: 141917.

[25] M M Wang, X H Gao, L Y Song, et al. Hydrogen trapping and electrochemical corrosion behavior of V–N microalloyed X80 pipeline steels consisting of acicular ferrite and polygonal ferrite. *Journal of Iron and Steel Research International*, 2022, 29(10): 1683–1693.

[26] Q B Yan, T Xue, S F Liu, et al. A comparative study of surface characterization and corrosion behavior of micro-arc oxidation treated Ti–6Al–4V alloy prepared by SEBM and SLM. *Journal of Iron and Steel Research International*, 2023, 30(1): 165–175.

[27] Y X Qiao, X Y Wang, L L Yang, et al. Effect of aging treatment on microstructure and corrosion behavior of a Fe–18Cr–15Mn–0.66N stainless steel. *Journal of Materials Science & Technology*, 2022, 107: 197–206.

[28] B Hirschorn, M E Orazem, B Tribollet, et al. Determination of effective capacitance and film thickness from constant-phase-element parameters. *Electrochimica Acta*, 2010, 55(21): 6218–6227.

[29] W L Liu, Q Y Wang, J Hao, et al. Corrosion resistance and corrosion interface characteristics of Cr-alloyed rebar based on accelerated corrosion testing with impressed current. *Journal of Materials Research and Technology*, 2023, 22: 2996–3009.

[30] P P Wang, H T Jiang, Y J Wang, et al. Role of trace additions of Ca and Sn in improving the corrosion resistance of Mg-3Al-1Zn alloy. *International Journal of Minerals, Metallurgy and Materials*, 2022, 29(8): 1559–1569.

[31] Z B Wang, H X Hu, Y G Zheng. Evaluation of the dissolved oxygen-related electrochemical behavior of pure titanium in acidic fluoride-containing solutions. *Journal of Solid State Electrochemistry*, 2016, 20(12): 3459–3471.

[32] L F Xie, W L Zhou. Salt spray corrosion behavior and pitting resistance of Ti-15V-3Cr-3Al-3Sn alloy evaluated using XPS, SKPFM, and electrochemical technique. *Journal of Solid State Electrochemistry*, 2022, 26(8): 1585–1603.

[33] T S Deng, X Y Zhong, M Zhong, et al. Effect of scandium on microstructure and corrosion resistance of Ti64 alloy in NaCl solution. *Materials Characterization*, 2023, 197: 112671.

[34] Z R Huang, H Xiao, J X Yu, et al. Effects of different annealing cooling methods on the microstructure and properties of TA10 titanium alloys. *Journal of Materials Research and Technology*, 2022, 18: 4859–4870.

[35] B X Su, L S Luo, B B Wang, et al. Annealed microstructure dependent corrosion behavior of Ti-6Al-3Nb-2Zr-1Mo alloy. *Journal of Materials Science & Technology*, 2021: 62: 234–248.

[36] G S Frankel, L Stockert, F Hunkeler, et al. Metastable pitting of stainless steel. *Corrosion*, 1987, 43(7): 429–435.

[37] M H Moayed, R C Newman. Evolution of current transients and morphology of metastable and stable pitting on stainless steel near the critical pitting temperature, *Corrosion Science*, 2006, 48(4): 1004–1018.

[38] F Y Gao, Y X Qiao, J Chen, et al. Effect of nitrogen content on corrosion behavior of high nitrogen austenitic stainless steel. *npj Materials Degradation*, 2023, 7: 75.

[39] L Q Yin, Y Y Liu, N W Dai, et al. Effect of hydrogen charging conditions on hydrogen blisters and pitting susceptibility of 445J1M ferritic stainless steel. *Journal of the Electrochemical Society*, 2018, 165(16): C1007–C1016.

[40] L Li, Y X Qiao, L M Zhang, et al. Effect of cavitation erosion induced surface damage on pitting and passive behaviors of 304L stainless steel. *International Journal of Minerals, Metallurgy and Materials*, 2023, 30(7): 1338–1352.

[41] H Feng, H B Li, X L Wu, et al. Effect of nitrogen on corrosion behaviour of a novel high nitrogen medium-entropy alloy CrCoNiN manufactured by pressurized metallurgy. *Journal of Materials Science & Technology*, 2018, 34(10): 1781–1790.

[42] H Y Ha, T H Lee, C S Oh, et al. Effects of combined addition of carbon and nitrogen on pitting corrosion behavior of Fe–18Cr–10Mn alloys. *Scripta Materialia*, 2009, 61(2): 121–124.

[43] H Liu, J J Yang, X Y Zhao, et al. Microstructure, mechanical properties and corrosion behaviors of biomedical Ti-Zr-Mo-xMn alloys for dental application. *Corrosion Science*, 2019, 161: 108195.

[44] B Roh, D D Macdonald. Effect of oxygen vacancies in anodic titanium oxide films on the kinetics of the oxygen electrode reaction. *Russian Journal of Electrochemistry*, 2007, 43(2): 125–135.

[45] Z B Wang, H X Hu, Y G Zheng, Synergistic effects of fluoride and chloride on general corrosion behavior of AISI 316 stainless steel and pure titanium in H_2SO_4 solutions. *Corrosion Science*, 2018, 130: 203–217.
[46] B Sivakumar, L C Pathak, R Singh. Role of surface roughness on corrosion and fretting corrosion behaviour of commercially pure titanium in Ringer's solution for bio-implant application. *Applied Surface Science*, 2017, 401: 385–398.
[47] Y Zhou, F Yang, Y Shao, et al. Electrochemical corrosion behavior of powder metallurgy Ti6Al4V Alloy. *Journal of Materials Engineering and Performance*, 2021, 30(1): 556–564.
[48] C E B Marino, E M de Oliveira, R C Rocha-Filho, et al. On the stability of thin-anodic-oxide films of titanium in acid phosphoric media. *Corrosion Science*, 2001, 43(8): 1465–1476.